MODELING SURFACE DEFORMATIONS AND HINGING REGIONS IN REINFORCED CONCRETE BRIDGE COLUMNS

By

Zeynep Firat Alemdar
Adolfo Matamoros
JoAnn Browning

A Report on Research Sponsored by

National Science Foundation Grant #0532084, Grant #0618804,
and KU Transportation Research Institute

Structural Engineering and Engineering Materials
SL Report No. 11-2
August 2011

THE UNIVERSITY OF KANSAS CENTER FOR RESEARCH, INC.
2385 Irving Hill Road – Campus West, Lawrence, Kansas 66045

ABSTRACT

A high-resolution model of a bridge column was developed using the computer program ABAQUS and the accuracy of the model was evaluated for the displacement field and the rotations of a bridge system subjected to biaxial shake-table loading. The effect of simulation parameters (reinforcing bar slip within the joint and stiffness degradation of the concrete) was studied to determine the goodness-of-fit of the displacement and rotation fields recorded during the dynamic response. A Fourier Domain Error Index analyses showed that yield stress of the reinforcement and the boundary conditions of the column submodel were important parameters, and the damage and stiffness degradation parameters were not as important for the goodness-of-fit of the finite element model. The computed rotations at the plastic hinge regions near the beam caps had the best correlation.

Keywords: reinforced concrete bridge column; finite element modeling; photogrammetry; earthquake loading; frequency domain error.

ACKNOWLEDGEMENTS

This project gratefully acknowledges the support of NSF grant #0532084, Joy Pauschke Program Director. The assistance and support of Prof. Saiid Saiidi, Graduate Research Assistant Roby Nelson, the entire staff of the research facilities at the University of Nevada Reno, Graduate Student Nick Hunt at University of Kansas, and Eric Sammarco at University of Texas at Austin are also gratefully acknowledged. Additional support from the National Science Foundation under award number # 0618804 through the Pacific Earthquake Engineering Research Center (PEER) is gratefully acknowledged.

TABLE OF CONTENTS

TABLE OF FIGURES

TABLE OF FIGURES

1 INTRODUCTION

Reinforced concrete bridge systems are designed with the objective of keeping inelastic deformations within the columns and away from the superstructure. For this reason accurate representation of the behavior of bridge columns in the inelastic range of response is important for the development of computer models that evaluate the performance of bridge systems under earthquake events. Understanding the spread of inelastic deformations at various stages of loading is also important to quantify the expected progression of damage and to estimate the deformation at which loss of lateral load capacity takes place. This is a particularly difficult problem when the structure is subjected to multiaxial loading, or when the structural components have a complex geometric shape.

1.1 FINITE ELEMENT SIMULATIONS OF REINFORCED CONCRETE COLUMNS SUBJECTED TO LOAD REVERSALS

A number of studies have explored the use of the finite element method to simulate the nonlinear response of reinforced concrete columns subjected to repeated load reversals. Early studies [1] focused on the development of computing platforms, material models, and solution algorithms that could be used to overcome the convergence problems posed by the nonlinear behavior of concrete. As CPU performance has improved, models have increased in size and complexity. More recent studies [2, 3] have focused on the validation of more complex finite element models, investigating the implementation of more sophisticated material models and element meshes.

1.2 OBJECTIVE AND SCOPE

The primary objective of this study was to develop a high-resolution model of a bridge column and to evaluate the accuracy of the model for estimating the displacement field that was recorded during the dynamic test of a bridge system under biaxial loading. A parametric study was conducted focusing on the effect of simulation parameters (reinforcing bar slip within the joint and stiffness degradation of the concrete) on the goodness-of-fit of the displacement and rotation fields recorded during the dynamic response.

1.3 RESEARCH SIGNIFICANCE

Engineers need guidance on finite element modeling parameters and analysis techniques that lead to accurate simulations of member behavior. This problem is of greater significance when modeling reinforced concrete under cyclic loading due to the highly nonlinear nature of the material response and the difficulties faced in achieving convergence. Computer models that yield accurate estimates of deformation throughout the member can be used to track the spread of inelastic deformations, rotations, and damage indicators throughout the entire loading history of a bridge system. Furthermore, the type of model developed in this study can account for complex axial load-flexure-shear-torsion interactions, and is applicable to columns with complex geometries that are subjected to biaxial or triaxial displacement histories.

The test column that was used to derive the model had complex boundary and loading conditions that uniquely supplement the current understanding of concrete

structural systems. The test column had a circular shape and was embedded in a cap beam and foundation block with rectangular cross-sections. Further complicating the analysis under biaxial loading, the superstructure support at the top of the pier frame allowed the column to rotate about the axis of the cap beam while the cap beam restrained it from rotating about the orthogonal axis. The change in geometric shape at the joints coupled with the biaxial nature of the loading and the boundary conditions make it very difficult to calculate the stress and displacement fields within the column and the joint.

Another unique aspect of this study was that the surface deformation map of the test column was recorded [4] during a series of earthquake simulator trials and used to quantify the accuracy of the model. Video cameras were used to record the movement in space of two grid systems applied to the surface of one of the columns of the bridge during earthquake shaking. The displacements at discrete points were later reduced from the pictures recorded by the cameras.

2 DESCRIPTION OF FOUR-SPAN LARGE SCALE REINFORCED BRIDGE TEST

The reinforced concrete bridge system was tested at the UNR laboratory under a sequence of uniaxial and biaxial earthquake trials with increasing intensity [5]. The test specimen, shown in Fig. 1, consisted of a four-span reinforced concrete bridge with end abutments. The specimen was approximately a quarter-scale representation of a bridge with two interior and two exterior spans that were 29 ft (8840 mm) and 24.5 ft (7470 mm) in length, respectively. The total length of the bridge system was approximately 110 ft (33528 mm). The clear heights of the bents were 5, 6 and 7 ft (1524, 1830, and 2130

mm), with the tallest bent in the middle (Bent 2). The measured compressive strength of the concrete that was used in the bridge (excluding the post-tensioned slab) was 6.7 ksi (46.2 MPa) and the reinforcing cage was fabricated using Grade 60 ASTM A706 (414 MPa) [6] deformed bars. The superstructure consisted of a post-tensioned solid slab both in the longitudinal and transverse directions. The bridge also had abutment seats at both ends that were driven in the longitudinal direction by dynamic hydraulic actuators to simulate the gap closure and impact at the abutments, and some of the test trials were conducted with SMA restrainers at the deck-abutment interface [7].

The displacement field was recorded at the top and bottom hinging regions of the east column of Bent 3 (Figs. 1 and 2). This column was 72 in. (1829 mm) long and 12 in. (305 mm) in diameter, with a 0.5 in. (13 mm) concrete cover. The column reinforcement consisted of 16 No. 3 (16-10M) longitudinal bars equally spaced around the perimeter of the column. The cap beam had a cross section of 15 by 15 in. (381 by 381 mm), with a total length of 98 in. (2.490 m). The ground motions used in the test trials were the scaled components of the Century City Country Club record from the 1994 Northridge, California earthquake. This earthquake record was used in a total of 13 trials, six of them with the bridge subjected to a single component in the longitudinal direction and seven trials subjected to both components. Trials were conducted with increasing amplitude with the goal of monitoring the progression of damage from pre-yield to failure.

Two different grids were created to track the displacements of the columns during shaking (Fig. 2). The grid systems were created by first spray-painting the column black to obtain a solid dark background. The lines and squares were lightly traced with a pencil over the dark background, and then filled using a single stencil and white paint. The

bottom grid had vertical and horizontal lines spaced irregularly around the face of the circular column. The top grid used a different configuration composed of lines and squares arranged so the spacing of the lines in the bottom grid would be similar to those at the top. The intersections of the thick vertical and horizontal lines in both regions were numbered as shown in Fig. 2 [8] and used as reference points to extract the displacement measurements on the surface of the column from the digital images following a process described elsewhere [4].

An aluminum tower was erected to support the cameras used to track the motion of the column during the sequence of trials. DXB-9212EF model Starlight 600 TVL high resolution cameras with black-white recording properties were placed on each level of the tower, with two cameras aimed at each grid. Video zoom lenses with focal length ranging from 60 to 300mm and minimum and maximum apertures of f/5.6-f/4 were used in the cameras to capture the motion of the grid surfaces shown in Fig. 2. Two monitors (two channels for each monitor) were set up to show the field of view of the cameras during the tests. The distance between the east column of Bent 3 and the instrumentation tower was 288 in. (7315 mm). The angles from the left and right cameras to the column were 73.58° and 44.97° on the horizontal plane as shown in Fig. 3, respectively. The displacements from photogrammetric measurements were obtained along the direction of the focal plane and compared with the combined displacements of transverse and longitudinal displacement transducers on the superstructure of the bridge.

3 FINITE ELEMENT MODEL OF THE BRIDGE COLUMN

A three-dimensional finite element model of the east column of Bent 3 was developed using the finite element software ABAQUS [9]. The model consisted of one half of the two-column pier frame system, including the east column, a 23-in. (584-mm) segment of the cap beam, and the footing (Fig. 4). The model had a total of 11,750 elements, and the response was analyzed using the implicit static general solution scheme with automatic stabilization. Simulations were performed on a Linux computational cluster with a total of 384 processors. Runs were performed using a maximum of 12 processors and took approximately four days to complete for a single test trial.

3.1 MATERIAL MODELS

In order to reduce the computational demand, concrete in the cap beam and the foundation block was modeled as a linear-elastic material. These two structural elements had much larger capacity than the column and experienced no observable damage during the test trials. Concrete in the column and in the connections was modeled using the damage plasticity model implemented in ABAQUS [9]. Two different sets of material properties were defined for the concrete in the core and the shell, to account of the effects of confinement provided by the spiral reinforcement. The stress-strain curve in compression for the concrete in the core was defined based on the Mander unified stress-strain model under monotonic loading at slow strain rates [10], shown in Fig. 5. The maximum strain was assumed to be 0.1, similar to the value of 0.06 that was used by [11, 12, and 13] in their research studies. The dynamic magnification factors used in the analysis followed the recommendations of Mander [10], who performed regression

analyses of the experimental results obtained by Watstein [14] with plain concrete specimens of different strengths. The compressive strength of concrete under dynamic loading $(f'_{co})_{dyn}$ was calculated using a dynamic amplification factor (D_f) as follows:

$$(f'_{co})_{dyn} = D_f \; f'_{co} \tag{1}$$

where f'_{co} is the quasi-static compressive strength of concrete in MPa (1 MPa=145 psi) and D_f = dynamic amplification factor defined by Eq. (2).

$$D_f = \frac{1+\left[\dfrac{\varepsilon_c}{0.035(f'_{co})^n}\right]^{1/6}}{1+\left[\dfrac{0.00001}{0.035(f'_{co})^n}\right]^{1/6}} \tag{2}$$

In Eq. (2) ε_c= rate of strain in s^{-1} and n = 2.

Previous work investigating the numerical modeling [15, 16] and experimental testing of full-scale models [17] of reinforced concrete structures concluded that the maximum strain rate in reinforced concrete structures subjected to severe earthquake ground motion ranged between 0.001 and 0.25 strain per second. A maximum strain rate of 0.05 strain per second was adopted.

The elastic modulus under dynamic loading $(E_c)_{dyn}$ was calculated as

$$(E_c)_{dyn} = D_f \, E_c \tag{3}$$

where D_f = dynamic amplification factor defined by Eq. (2) with n = 3.

The modulus of rupture of the concrete was taken as $4\sqrt{f'_c}$ (in units of psi). The softening effect of concrete in uniaxial tension, after cracking, was evaluated as a parameter using equations proposed by [18], [19], and [20] (Fig. 5). The Bhide tension model [18] with a cracking angle of 35° was chosen for this study because it provided the best performance. Tensile behavior was specified in terms of a stress-displacement

relationship calculated on the basis of the tension model and an average crack spacing [21]. This technique was adopted with the objective of reducing the sensitivity of the response to mesh size. The analyses were performed assuming linear elastic behavior of the cap beam and foundation block because the stiffness and yield moment of the cap beam (I_g = 4200 in^4, M_n^+ = 210 k ft, and M_n^- = 180 k ft) were significantly higher than that of the column (I_g = 1020 in^4 and M_n = 45 k ft).this assumption is also supported by a much large load capacity in the cap beam and foundation with respect to the column, and an absence of damage in these large-capacity elements. The flexural stiffness of the cap beam was calculated assuming that there was an inflection point at the center of the cap beam. The moment of inertia of the cap beam was varied as a parameter approximately between the cracked (2000 in^4, 8x10^8 mm^4) and gross moments of inertia (4200 in^4, 1.75x10^9 mm^4) of the cross section. Additional analyses were performed assuming that the cap beam was infinitely stiff.

A uniaxial steel model with combined isotropic and kinematic hardening properties was used to simulate the behavior of the longitudinal steel. Isotropic parameters were defined on the basis of a typical stress-strain relationship for ASTM A706 Grade 60 steel [6]. The strength of the steel was adjusted to account for the effect of strain rate under dynamic loading through the use of a dynamic magnification factor. Experimental data from ASTM A615 steel [17] showed that for strain rates consistent with earthquake loading the dynamic yield stress was approximately 10 percent larger than the static yield stress. According to research by Manjoine [22], the increase in ultimate strength of mild structural steel associated with increased loading rate was

approximately 4%. Several studies [16, 23, and 24] indicate that increased strain rate had relatively little effect on the elastic modulus of steel.

Kinematic hardening properties were defined to include cyclic strain softening on the basis of experimental results by Ma et al. [25]. The material model was calibrated by performing simulations of a reinforcing steel bar subjected to repeated load reversals in which material behavior was modeled with the combined hardening algorithm. The stress-strain curve of a single element near the center of the steel bar is compared with the experimental data reported by Ma et al. in Fig. 6, which shows that there was a close match between the results from the computational model and the experimental results.

3.2 FINITE ELEMENT MESH

The concrete mesh consisted of quadratic brick elements with twenty integration points. The cap beam was modeled in two different segments. The first segment, starting at the edge of the cap beam and having a length equal to twice the distance from the edge of the beam to the center of the column, was modeled using solid elements (Fig. 4). The second segment extended from the end of the first segment to the center of the pier frame, and was modeled using a single rotational spring element. The spring element was rigidly attached to a thin but infinitely stiff layer of transition elements at a point located at the center of the right face of the cap beam (Fig. 4).

The circular column and the two joints with the cap beam and the footing were modeled using 3D continuum 8-node brick elements. The brick elements had twenty integration points and a reduced integration scheme was used to reduce the computation time for the analysis. A coarser mesh with 4-in. (102-mm) elements was used in the

remainder of the cap beam and the footing because these two components experienced no observed damage. The solid element mesh for the cap beam-column connection, the column-footing connection, and the circular column was generated taking into account the location of the longitudinal reinforcement (Fig. 4). Concrete in these solid elements was modeled using the damage plasticity model in ABAQUS [9]. Longitudinal reinforcement and transverse steel hoops were modeled using 1D 2-node ABAQUS wire elements and linked to the edge of the solid elements using embedded constraints. The longitudinal steel had a cross-sectional area of 0.11 in.^{2} (71 mm^2) and transverse hoops had a cross sectional area of 0.029 in.^{2} (18.7 mm^2) evenly distributed every 1.25 in. (32 mm) along the height of the column.

Models with different element sizes in the connections and the column were analyzed to study the sensitivity of the load-displacement relationship to mesh size. Computed load-displacement relationships under monotonically increasing lateral load for various mesh configurations were compared with load-displacement curves calculated using Response 2000 (MCFT) [26] and simple models based on moment-curvature relationships. The response of models with mesh sizes of 3 in. (76 mm), 1 in. (25 mm), and 0.5 in. (13 mm) along the top and bottom hinging regions of the column and 4 in. elsewhere are shown in Fig. 7. This study showed that the load-deformation curve of the column was sensitive to mesh size, with smaller mesh sizes resulting in lower column stiffness. The curve corresponding to moment-curvature includes only the flexural component of the displacement, while the curve computed based on the MCFT includes displacement components related to flexure and shear, but does not account for the displacement component related to slip of the reinforcement (which was shown to be

relatively small in this case given the large embedment of the bars and the highly confined nature of the joint). Figure 7 shows that the 1-in. (25-mm) mesh model provided the closest match to the force-displacement response prior to yielding computed using the MCFT [26], with slightly larger displacements near yield that account for the effect of slip of the reinforcement.

Because the longitudinal reinforcement of the column was deeply embedded into the cap beam and into the foundation block, and both the cap beam and the foundation block provided significant confinement to the concrete in the joints, simulations presented in this paper were performed by modeling slip solely through the softening effect of the concrete in tension. This assumption is consistent with the damage pattern observed in the specimens, which experienced negligible damage in the cap beam-to-column and foundation-to-column connections. Other techniques for modeling slip explicitly such as the use of zero-length slip elements in the bars, the use of short debonded regions at the edges of the column, and the use of cohesive layers surrounding the bars in the joint region were also evaluated [27] but were found to have a negligible effect on the goodness-of-fit of the model.

3.3 LOAD AND BOUNDARY CONDITIONS

The axial load on the column was computed based on the tributary area of the column and consisted of an imposed weight of 47.2 kips (210 kN) applied as a uniform pressure at the surface of the cap beam in the FE model (Fig.4). One half of the pier frame was analyzed by imposing the two lateral components of the earthquake simulator displacement at the bottom surface of the footing and the recorded displacement

components recorded with LVDTs at the top of the column, in the cap beam. The top of the footing was restrained from vertical motion also (Fig. 4) to simulate the effect of postensioned rods and steel plate washers used to tie the footing to the table.

As previously mentioned, the bridge was subjected to a sequence of test trials with increasing ground motion amplitude. A simulation of the sequence of thirteen major trials in the computer platform available would take approximately 50 days to run, which would make a parametric study impractical to perform. The comparisons presented in this paper correspond to single runs of test trial 4D, which was selected for discussion because it imposed a biaxial motion on the bridge and represented the first trial in which significant inelastic deformations were observed in both directions of the bridge response. Recorded values of the transverse displacement of Bent 3 (measured with displacement sensor DT7) are shown in Fig. 8. Also, because both grids were relatively intact at the end of trial 4D it was simple to reduce a complete data set. This was not the case for subsequent trials. A simulation with all trials was performed and results show that computed rotations and displacements were similar to those computed on the basis of trial 4D alone.

The two components of the ground motion imposed on the bridge during test trial 4D had peak ground accelerations of 0.5*g* in transverse direction and 0.6*g* in the longitudinal direction, and induced a maximum drift ratio on the column of approximately 4% in the longitudinal direction and 3% in the transverse direction.

3.4 SOLUTION ALGORITHM

One of the most challenging aspects of the type of simulations performed in this study is that the descending branch of the stress-strain relationships for concrete in compression and tension can lead to great difficulties achieving numerical convergence when implicit solution algorithms are employed. When inelastic behavior occurs the descending branch of the stress-strain curve for concrete can lead to unstable behavior, that is, instances in which strain energy must be released from the system as deformation increases due to loss of strength in the material. This problem is more pronounced when concrete is unconfined or poorly confined causing the slope of the descending branch to become steeper, as in the case of the concrete in the shell of the column.

ABAQUS offers several solution algorithms for problems with unstable nonlinear behavior, based on both implicit and explicit algorithms. Implicit algorithms offer greater accuracy at a much greater computational cost and greater difficulty achieving convergence. Depending on the severity of the instability, a model such as the one evaluated in this study may be approached as a pseudostatic problem in which a small amount of damping is introduced to facilitate convergence when unstable behavior arises. If the instability is too severe, this technique requires relatively large damping forces to achieve convergence, which cause the computed solution to deviate significantly from the true solution. In such instances, an implicit solution requires a dynamic analysis instead. An implicit static solution algorithm was chosen because it provided greater accuracy in estimating the displacement field of the column and required significantly less CPU time than an implicit dynamic solution algorithm.

Although the concrete in the core of the column is well confined, and consequently less prone to cause convergence problems, the concrete in the shell presented a significant challenge. Because the most severe convergence problems are posed by the concrete in the shell, which has a relatively small effect on the overall response of the column, convergence was achieved without meaningful loss in precision by setting the dissipated energy fraction of the automatic damping algorithm to 0.002 and relaxing the convergence criteria for the ratio of largest residual to average flux norm and the ratio of largest solution correction to the largest incremental solution value.

3.5 PARAMETERS OF THE FINITE ELEMENT STUDY

Several researchers [28, 29, 30, and 31] have developed expressions for the spread of plasticity in columns by adopting as a limit state the deformation corresponding to the loss of lateral load capacity. In those studies, loss of lateral load capacity is defined as the point in the load-deflection or moment-deflection relationship corresponding to a reduction of 20% from the maximum moment or shear force recorded in an experiment. Studies have concluded that factors such as strain penetration [29, 31, and 32], axial load demand [30, 33], and shear span-to-depth ratio [30, 34, 35, and 36] have a significant effect on the spread of plasticity. Many of these parameters were fixed in the experimental sets that are available, which limited the ability to evaluate their effect on the accuracy of the model. For this reason, parameters of the study focused on material models for the steel and concrete and the boundary conditions. Model parameters included the yield stress of the reinforcement, the use of various techniques to simulate

the effects of slip of the reinforcement, the damage function coefficients for concrete under cyclic loading, and the stiffness of the cap beam.

4 EVALUATION OF RESULTS FROM THE FINITE ELEMENT MODELS

Figure 9 shows a comparison between displacement values inferred from video images and the optimum finite element model at the point of peak displacement demand on the column. Lateral displacement signals used for comparison with digital imaging results in this paper were calculated along the direction of an axis perpendicular to the axis between the column and the left camera with the positive direction having an orientation of N15.25°W with respect to the longitudinal axis of the bridge.

Direct comparisons of the displacement field at peak response, such as the one depicted in Fig. 9, are a useful measure of the accuracy of the FE model at a single point in time. A systematic evaluation of the accuracy of the various models over the duration of the entire trial was performed by comparing computed displacement and rotation signals at several locations throughout the column with signals that were recorded with displacement sensors and video images. In comparing FEA and digital imaging results, column rotations were computed about a horizontal axis spanning between the column and the left camera with an orientation of N74.75°E with respect to the longitudinal axis of the bridge. As shown in Fig. 2, LVDT sensors were anchored to the column to measure rotations relative to the cap beam in directions perpendicular to and parallel to the axis of the cap beam. Comparisons of column rotations between FEA and LVDT results were performed based on values computed about an axis perpendicular to the axis

of the cap beam. These rotations were deemed to have more significance between the two direct measurements recorded with LVDTs due to the relatively large stiffness and strength of the cap beam relative to those of the column, and because the top of the column was essentially unrestrained from rotation about the axis of the cap beam.

Vertical displacement signals from LVDTs were used to interpolate the vertical displacements at grid points and at the surface of the column. Vertical displacement comparisons between FEA and digital imaging signals were performed on the basis of absolute displacement signals, while comparisons between FEA and LVDT signals were performed on the basis of the relative displacements between the two column elevations monitored by the LVDTs.

A quantitative technique based on the Frequency Domain Error index (FDE), developed by Dragovich and Lepage [37], was used to compare measured (or inferred) and computed response quantities. The FDE index uses the Fourier spectra to compare the composition of the two signals, with differences between the Fourier coefficients increasing the value of the error index. The FDE index quantifies the goodness-of-fit of the amplitude and phase of two signals and its value ranges between 0 and 1, where zero indicates a perfect correlation. The amplitude error is a measure of the difference between the norm amplitudes of the Fourier coefficients of the two response signals, while the phase angle error is a measure of the difference in the angle that the resultant vectors make with respect to the real axis in the real-complex plane. Dragovich and Lepage concluded that an FDE value of 0.75 or higher represented a poor correlation, and that an FDE value of 0.25 or lower represented a very good correlation.

The range of frequencies to be evaluated was selected to be between 0.5 Hz and the Nyquist frequency $f_n = 1/(2\Delta_t)$, where Δ_t was the sampling interval of the data series. In the case of the video images the sampling rate was 30 frames per second, while in the case of the FEA and the analog sensor data the time interval of the recorded data was 0.007812 seconds. The difference in time increments was addressed by resampling the data signals from the FEA and analog sensors using linear interpolation so that all signals would have a same sampling rate of 30 points per second.

The displacement field computed with the finite element model had input data recorded using analog sensors, while the measured displacement field on the surface of the column was inferred from digital video images. Because the two sensors systems acted independently of each other, a direct comparison of the signals obtained with each type of sensor during trial 4D showed the magnitude of the experimental error introduced by differences in the precision of the two sensor systems, which is independent of the modeling assumptions. The time signal from the two sensor systems was synchronized by comparing the lateral displacements inferred from digital imaging at point 3, located near the bottom of the column, with the lateral displacement signal from the earthquake simulator. The synchronization was carried out in a two stage process that involved a first approximation by visual inspection followed by a series of FDE analyses to determine the time offset that would result in the lowest phase error. The best match between the displacements inferred from digital imaging and the earthquake simulator signal yielded FDE error indices of 0.04 for amplitude error and 0.12 for phase error, for a total error of 0.16. These error values show that there was an excellent correlation between the

displacements inferred from video images at the base of the column and the earthquake simulator signal.

A similar comparison was performed on the basis of FDE indices comparing the lateral displacement signals at the top of the column. The lateral displacements corresponding to grid Point 58 (Fig. 2), located at near top of the column, were compared with the combined components of the displacement transducers mounted on the bridge deck and the north abutment (DT7, DS1 and DS5 in Fig. 2). As shown in Fig. 2, the displacement transducers were separated from point 58 of the grid by a distance of 23 in. (584 mm). The FDE amplitude index between the two signals was calculated to be 0.09, and the phase angle error was calculated to be 0.31, for a total error of 0.40. These computed error values show that the correlation between digital imaging and the LVDT data at the top of the column was not nearly as good as that observed at the bottom of the column between the digital imaging data and the earthquake simulator signal. While is not possible to conclude with certainty that the larger discrepancy between sensor readings at the top of the column can be attributed to either one of the two sensor systems, flexibilities from anchors and attachment accessories as well as rotation of the cap beam introduce sources of experimental error in the analog sensor readings that do not affect the signal from the earthquake simulator nor the digital imaging. Regardless of the source of the error, it is important to keep in mind that a larger amount of sensor error is present in comparisons between digital imaging readings and displacements computed from FEA models at the upper column grid due to the larger discrepancy between sensor systems at that location.

4.1 AS-BUILT SIMULATIONS

A set of simulations was carried out with modeling assumptions intended to represent the as-built characteristics of the frame pier as closely as possible. Material properties were defined based on reported measured values (f'_c = 6.7 ksi and f_y = 64 ksi) [4] adjusted for rate effects as described previously in the paper.

Table 1 shows the FDE indices for comparisons between the computed lateral displacements at discrete points on the surface of the column (with analog sensor data as input) and the displacements at the same points inferred from the video images. Amplitude error indices show a better correlation for the bottom grid than at the top grid. While amplitude errors remained nearly constant throughout, phase error indices increased in magnitude as the height along the column increased. This is consistent with the direct comparison of the digital and analog sensor readings. Computed and inferred signals for Point 3 (near the bottom of the column in Fig. 2, with an amplitude error of 0.04 and a phase error of 0.12) and Point 58 (near the top of the column in Fig. 2, with an amplitude error of 0.09 and a phase error of 0.31), are plotted in Fig. 10 to illustrate the close similarity between the respective signals.

The vertical displacement history at the top and bottom hinging regions of the FE model were also compared with digital imaging data. The results of the FE model at points located 5 in. (127 mm) and 10 in. (254 mm) above the footing and below the cap beam were obtained and compared with the vertical displacement data reduced from video images. Table 2 lists the FDE indices for these comparisons. The amplitude error is indicative of a very close match between the two signals everywhere in the column while the phase error is indicative of a fair match between the signals everywhere in the

column. The calculated FDE indices show that the difference between the two signals was smaller at the top of the column than at the bottom of the column, and that calculated vertical displacements near the top of the column did not match measured values nearly as well as the calculated lateral displacements did. This is attributable to the accuracy of the imaging equipment that was utilized and the fact that the vertical displacements being measured were on the order of a few hundreds of an inch. Direct measurements of relative vertical displacements obtained with LVDTs were also available at discrete locations. A comparison between the relative vertical displacements calculated with the FE model and those measured with LVDTs is presented in Table 3. The results also show far better correlation at the top of the column than at the bottom of the column. It is important to note that absolute vertical displacements at points in the bottom grid are very small, which makes comparison of FEA vs. digital imaging data signals at these locations particularly sensitive to experimental error. FDE indices from LVDT-FEA comparisons at the top of the column had total error magnitudes on the order of 0.3, indicative of a very good match.

FDE error indices obtained by comparing rotation signals inferred from FEA and LVDT sensors are presented in Table 4. Computed rotation values show excellent correlation with the experimental data everywhere in the column, with the largest amount of error found in the top 5-in. (127-mm) segment of the column.

4.2 EFFECT OF THE YIELD STRENGTH OF THE REINFORCEMENT

Because there was no experimental data available to directly quantify the effect of strain rate on the yield stress of the reinforcement, the yield stress of the longitudinal

reinforcement was varied as a parameter in the FEA models. Simulations were performed using yield stress values of 64, 70, 75, and 80 ksi (441, 483, 517, and 552 MPa), corresponding to dynamic amplification factors of 0, 10%, 18% and 25%, respectively. The effect of yield stress on the goodness of fit of the model was evaluated by comparing lateral displacements, vertical displacements, and rotations at points located 5 in. (127 mm) and 10 in. (254 mm) from the edge of the column, where data was available both from video images and LVDT sensors. Cross-section rotations about an axis perpendicular to the axis of the cap beam were calculated at the locations of LVDTs 3ETR3 and 3ETR4 (5 in. or 127 mm below the cap beam), 3ETR5 and 3ETR6 (located at 12 in. or 305 mm below the cap beam), 3EBR7 and 3EBR8 (located 5 in. or 127 mm above the footing), and 3EBR5 and 3EBR6 (located at 12 in. or 305 mm above the footing). Error indices showed that the quantity most sensitive to yield stress was the vertical displacement at the top of the column. Figure 11 shows a comparison of the relative vertical displacement signals near the location of LVDT 3ETR4, located 5 in. (127 mm) below the cap beam, for the different values of yield stress used in the FE models. As shown in Fig. 11 the main difference between the signals was the residual relative displacement, with LVDT 3ETR4 indicating a very small shortening of this segment of the column at the end of the test trial (approximately 0.01 in. or 0.25 mm) while the FE models indicated various degrees of residual lengthening (ranging between 0.01 and 0.08 in., or 0.25 mm and 2.03 mm) due to the nonlinear deformations of the steel bars. These graphs show that a yield stress exceeding 80 ksi (552 MPa) would be needed to obtain the best match in terms of vertical displacement.

Figure 12 shows that FDE indices for the cross-sectional rotations perpendicular to the cap beam at elevations 5 in. (127 mm) and 12 in. (305 mm) below the cap beam and above the footing. FDE indices in general were insensitive to yield stress and were indicative of an excellent correlation. The two error indices most sensitive to yield stress were those corresponding to the vertical displacement signal at the top of the column and the rotation signal in the 5-in. (127-mm) segment of the column directly above the footing. For both of these signals the correlation had a tendency to improve with increasing yield stress.

4.3 EFFECT OF THE FLEXURAL STIFFNESS OF THE CAP BEAM

One of the limitations of the model is that in order to keep the computational demand to a reasonable level only one half of the pier-frame was modeled, and the cap beam was modeled with a very simple linear-elastic element. As discussed previously, the flexural stiffness of the cap beam was varied during the calibration of the model to investigate the effect of beam flexibility on the goodness of fit of the displacement field of the column. For the case of gross section properties the flexural stiffness of the spring K_g was calculated to be approximately $3x10^9$ lb-in. ($3.4*10^8$ N-m) and for the fully cracked condition it was 10^9 lb-in. ($113*10^6$ N-m). The stiffness of the spring element was varied from 10^8 lb-in. ($113*10^5$ N-m) to 10^9 lb-in. ($113*10^6$ N-m) in order to allow for additional flexibility from slip of the reinforcement. To complement the data set, simulations were performed in which the cap beam was restrained from rotating as if it were infinitely stiff. The yield stress of the column reinforcement was varied also with values of 68 and 75 ksi (469 MPa and 517 MPa), corresponding to dynamic amplification

factors of 6.25% and 17%, respectively, in order to find the optimum combination of parameters.

Comparisons of goodness-of-fit were performed in terms of computed rotations about an axis perpendicular to the axis of the cap beam, at points located 5 in. (127 mm) and 12 in. (305 mm) above the footing and below the cap beam. FDE error indices are presented in Table 5. In general, higher beam stiffness values led to better correlations at the top hinge region of the column. The opposite was true for the bottom hinge, where lower stiffness values led to better correlation between measured and computed values. The goodness-of-fit of the rotations at the bottom hinge was more sensitive to the flexural stiffness of the cap beam than that at the top hinge, and the largest error index was found for the total rotation in the bottom 12-in. (305-mm) segment of the column. Index errors (Table 6) were very similar for yield stresses of 68 ksi (469 MPa) (Table 6) and 75 ksi (517 MPa), with the average being slightly lower for the model with a yield stress of 75 ksi (517 MPa). For this reason the model with a flexural stiffness of 10^8 lb-in. ($1.1*10^7$ N-m), and a yield stress of 75 ksi (517 MPa) was selected as the optimum model.

4.4 EFFECT OF STIFFNESS DEGRADATION PARAMETERS

Reinforced concrete structures subjected to repeated load reversals into the nonlinear range of response experience progressive damage and a reduction in stiffness. When the post-peak compressive stress or tensile crack displacement increase, the material sustains non-recoverable damage, and the stiffness of the material is reduced after a load reversal occurs. The damage variables d_c and d_t are used in the concrete plasticity model in ABAQUS to simulate stiffness degradation by reducing the elastic

modulus after a load reversal by a factor of (1-*d*). These two stiffness degradation parameters are defined as a function of the inelastic compressive strain and the tensile crack displacement, respectively, so that the reduction in stiffness increases with inelastic deformation. In this study, the compression stiffness degradation parameters for core and cover concrete were defined as exponential functions dependent on the plastic component of the compressive strain. Equations 4 and 5 were used for core and cover concrete respectively:

$$d_c = 1 - e^{-30\varepsilon_{pl}} \tag{4}$$

$$d_c = 1 - e^{-160\varepsilon_{pl}} \tag{5}$$

where ε_{pl} is the plastic component of the compressive strain. The tension stiffness degradation parameter d_t was defined as a linear function in which a 50 percent reduction of the elastic stiffness was assumed to occur when the critical crack bandwidth value was reached, and 98 percent of the elastic stiffness when the critical crack bandwidth was doubled. These relationships were found to provide reasonable results in a previous study on column behavior [21].

For the case of cyclic loading, the damage variables d_c and d_t in the concrete damage plasticity model in ABAQUS are modified through the use of weight factors w_c and w_t to account for the stiffness recovery effect when the direction of loading changes. The modulus of elasticity is then reduced by a factor of [1 - (1-*w*) *d*], were a *w* value of 1 corresponds to full recovery of the elastic modulus and a value of 0 signifies a reduction by a factor of (1-*d*). The compression stiffness recovery parameter (w_c) was varied between 0.5 and 1.0, where a value of 1.0 implies that as cracks close during load

reversal the compression stiffness will be completely recovered. The tension stiffness recovery variable (w_t) was varied between 0 and 1.0.

FDE indices for rotations with several combinations of compression and tension stiffness recovery parameters evaluated are summarized in Table 7. Although the rotation FDE indices were not very sensitive to these parameters, the best correlations were found for a combination of recovery variables w_c =0.8 and w_t =1.0. A similar trend was observed for the case of vertical displacements. These values of stiffness recovery parameters were used on all other analyses.

Computed damage patterns at the end of the test trial, quantified in terms of the damage variables d_c and d_t, are shown in Fig. 14 and were found to be consistent with observed damage in the column.

5 COLUMN BEHAVIOR

A finite element analysis with the optimum model parameters showed that inelastic deformations of the column during trial 4D were concentrated almost entirely at the bottom of the column. Displacement profiles for two points in time corresponding to the largest deformation demands on the column are presented in Fig. 15. The corresponding curvature profiles are presented in Fig. 16 and the strain demand in the various reinforcing bars is presented in Fig. 17. All quantities are shown about axis in the direction of the peak displacements. These figures show that in the column member analyzed, which is a typical bridge column with relatively low axial load demand, column response was driven primarily by the deformation of the longitudinal

reinforcement. Finite element analyses of the bridge column during trial 4D, with peak ground accelerations of 0.5*g* in transverse direction and 0.6*g* in the longitudinal direction, indicate that the strain demands in the longitudinal reinforcement exceeded the elastic range in the lowest 25-in. (635-mm) segment of the column, which corresponds to approximately 2 times the diameter of the column. The inelastic strains in the longitudinal bars extended approximately 12 in. (305 mm) or approximately 1 column diameter or 32 longitudinal bar diameters into the joint. Computed curvature demands exceeded the yield curvature over a shorter segment of approximately one half the diameter of the column (Fig 16). Computed strain demands on the reinforcement show that the highest strain demands on the reinforcement occurred over the same bottom 6-in. (152-mm) segment of the column where curvature exceeded the nominal yield curvature, although inelastic behavior extended over a distance 4 times larger.

6 SUMMARY AND CONCLUSIONS

An FE model of a bridge column was created using a widely available computer program and concrete plasticity model. The computational demand was maintained at a reasonable level by modeling nonlinear behavior only in areas of the bridge pier where inelastic deformations were expected and shown to take place. Simulations that resulted in a close representation of the experimentally measured displacement field of the column under dynamic biaxial loading were performed using an implicit static solution algorithm with stabilization, which was found to be significantly more efficient than an implicit dynamic algorithm for this type of model.

Results showed that in spite of using material modeling techniques intended to minimize the effect of mesh sensitivity, the computed load-deformation response of the column was indeed sensitive to mesh size, with column stiffness decreasing with element size. A model that correlated well with experimental results from a dynamic test under biaxial loading was developed by selecting the mesh configuration so that the load-deformation response under monotonic loading would match the response calculated with much simpler models based on the modified compression field theory and simple moment-curvature relationships.

The deformed shape of the bridge column under biaxial earthquake loading computed with the FE model closely followed the deformed shape of the column reduced from the video imaging data, for a test trial that induced a maximum drift ratio on the column of approximately 4%. The parametric study showed that the goodness-of-fit of the computer model, quantified by the Fourier Domain Error Index, was most sensitive to yield stress of the reinforcement and the boundary conditions of the column submodel, and was not very sensitive to the damage and stiffness degradation parameters. The best correlation was obtained for the computed rotations at the plastic hinge regions. Higher signal errors were obtained by comparing lateral displacements, and the highest signal errors were associated with the vertical displacement signals. Error indices increased as the magnitude of the displacements decreased, which was expected due to the experimental error inherent to the sensors and measuring techniques used to record the displacements.

As computer CPUs become more powerful the use of models such as those developed in this paper becomes more accessible to engineers. The value of this type of

models lies in the ability to analyze very complex structural problems such as simulating the nonlinear behavior of members subjected to multiaxial dynamic loading. Given that a detailed deformation map of the column was recorded during the test, the study shows the value use of modeling techniques and analysis algorithms that accurately represent the displacement field within columns subjected to complex loading conditions.

REFERENCES

1. Ignatakis, C., Stavrakakis, E., and Penelis, G., 1989, Analytical Model for Masonry Using the FEM, In C.A. Brebbia (ed.), Structural Repair and Maintenance of Historical Buildings, 511-523, Southampton: Computational Mechanics Publication.
2. Mostafaei, H., and Vecchio, F. J., (2008). "Uniaxial Shear-Flexure Model forReinforced Concrete Elements" ASCE Journal of Structural Enginering, 134(9), 1538-1547.
3. Hachem M. M., Mahin S.A., Moehle J.P. Performance of circular reinforced concrete bridge columns under bidirectional earthquake loading. Report No. PEER 2003/06, Pac. Earthq. Eng. Research Center, University of California at Berkeley, Feb. 2003, 490 pp.
4. Firat Alemdar Z., Browning J., Olafsen J. "Photogrammetric Measurements of RC Bridge Column Deformations", Journal of Engineering Structures, Vol. 33 Issue 8, pp. 2407-2415, August 2011.
5. Robert B. Nelson, M. "Saiid" Saiidi, and S. Zadeh (2007). "Experimental Evaluation of Performance of Conventional Bridge Systems" Center for Civil engineering Earthquake Research Report No. CCEER-07-04, University of Nevada.

6. ASTM, A. (2002). "706/A 706M-01 " Standard Specification for Low-Alloy Steel Deformed and Plain Bars for Concrete Reinforcement," ASTM International, West Conshohocken, Pa.
7. Padgett, J. E. and DesRoches, R. (2007). "Experimental Evaluation of a New Retrofit Device Using Shape Memory Alloys," *Proceedings of the 1st US-Italy Seismic Bridge Workshop*, Pavia, Italy, April 18-20, 2007.
8. Firat Alemdar Z., Browning J., Olafsen J., and Nick Hunt. 2008. "Monitoring RC Bridge Column Hinging With Photogrammetry", 14th World Conference on Earthquake Engineering, Bejing, China.
9. ABAQUS, Version 6.8-2, Simulia, 2009, http://www.simulia.com.
10. Mander J. B., Priestley M. J. N., and Park R. Seismic Design of Bridge Piers. Department of Civil Engineering Research Report 84-2, University of Canterbury, 483 pp. 1984.
11. Scott, B.D., Park, R., and Priestley, M.J.N. Stress-strain behavior of concrete confined by overlapping hoops at low and high strain rates. ACI Struct J 1982 V. 79 No. 1 pp. 13-27.
12. Spacone, E., Filippou, F., and Taucer, F. F. Fibre beam-column model for nonlinear analysis of r/c frames: part 1. formulation. Earthquake Eng. And Structural Dynamics, V. 25, 711-725, 1996.
13. Yassin, M. Nonlinear analysis of prestressed concrete structures under monotonic and cyclic loads. Ph.D. Thesis, University of California, Berkeley 1994.
14. Watstein, D. Effect of straining rate on the compressive strength and elastic properties of concrete. Am. Conc. Inst. J., 24(8), 729-744. 1953.

15. Wakabayashi, M. Design of Earthquake-Resistant Buildings. New York:McGraw-Hill, 1986.
16. Mahin, S.A., V.V. Bertero, M.B. Atalya, and D. Rea. Rate of loading effects on uncracked and repaired reinforced concrete members. Report UCB/EERC-72/09. Berkeley: EERC, University of California, 1972.
17. Hosoya, H. et al. Strain rate in the members of reinforced concrete frame structure during an earthquake and its effects. Journal of Structural and Construction Engineering (Transactions of AIJ) 499 (1997): 77-83.
18. Bhide, S. B., and Collins, M. P. Reinforced concrete elements in shear and tension. Publication No. 87-02, Department of Civil Engineering, University of Toronto, Jan. 1987, 308 pp.
19. Vecchio, F. J., and Collins, M. P. Response of reinforced concrete to in-plane shear and normal stresses. Publ. No. 82-03, Dept. of Civil Engineering, Univ. of Toronto. 1982.
20. Collins, M. P., and Mitchell, D. Prestressed concrete basics. Canadian Prestressed Concrete Institute, Ottawa. 1987.
21. Matamoros A., and Sammarco E., "Plasticity-Based Nonlinear Finite Element Analysis of Reinforced Concrete Columns with Inadequate Seismic Detailing", 9th U.S. National and 10th Canadian Conference on Earthquake Engineering, 2010.
22. Manjoine M.J., "Influence of Rate of Strain and Temperature on Yield Stresses of Mild Steel." Journal of Applied Mechanics 11 (1944): 211-218.

23. ACI Committee 439. Effect of steel strength and of reinforcement ratio on the mode of failure and strain energy capacity of reinforced concrete beams. ACI Journal 66 (3) (1969): 165-173.
24. CEB-FIP. CEB-FIP Model Code 1990: Design Code. London: T Telford, 1993.
25. Ma, S-Y.M., V.V. Bertero and E.P. Popov. Experimental and analytical studies of the hysteretic behavior of reinforced concrete rectangular and t-beams. Report No. EERC-76-2. Berkeley: EERC, University of California, 1976.
26. Response-2000. Reinforced concrete sectional analysis using the modified compression field theory. Version 1.0.5, last accessed 2010, http://www.ecf.utoronto.ca/~bentz/r2k.htm.
27. Firat Alemdar Z. Evaluation of plastic hinge regions in reinforced concrete bridge systems. Ph.D. dissertation, Lawrence (KS): the University of Kansas; 2010.
28. Priestley M. J. N., Park R. Strength and ductility of concrete bridge columns under seismic loading. ACI Structural J 1987 V.84 Issue 1. pp. 61-76.
29. Paulay T., Priestley M. J. N. Seismic design of reinforced concrete and masonry structures. John Wiley & Sons, Inc. 1992.
30. Bae, S. (2005), "Seismic Performance of Full-Scale Reinforced Concrete Columns", PhD Dissertation, the University of Texas at Austin, Austin, TX, 311 pp.
31. Berry, M., Lehman D. E., and Lowes L. N. (2008). "Lumped-Plasticity Models for Performance Simulation of Bridge Columns," ACI Structural Journal, V. 105, No. 3, May-June, pp. 270-279.

32. Mander J. B. (1983). “Seismic Design of Bridge Piers,” PhD Thesis, University of Canterbury, Christ Church, New Zealand.
33. Watson, S. and Park, R. (1994), “Simulated Seismic Load Tests on Reinforced Concrete Columns,” Journal of Structural Engineering, ASCE, V. 120, No. 6, June, pp. 1825-1849.
34. Sakai, K. and Sheikh, S.A. (1989). “What Do We Know about Confinement in Reinforced Concrete Columns? (A Critical Review of Previous Work and Code Provisions),” ACI Structural Journal, V. 86, No. 2, Mar.-Apr., pp. 192-207.
35. Tanaka, H. and Park, R. (1990). “Effect of Lateral Confining Reinforcement on the Ductile Behavior of Reinforced Concrete Columns,” Research Report 90-2, Department of Civil Engineering, University of Canterbury, Christchurch, New Zealand, June, 458 pp.
36. Bayrak, O. and Sheikh, S.A. (1997). “High-Strength Concrete Columns under Simulated Earthquake Loading,” ACI Structural Journal, V. 94, No. 6, Nov.-Dec., pp. 708-722.
37. Dragovich JJ., Lepage A. FDE index for goodness-of-fit between measured and calculated response signals. Earthquake Engineering and Structural Dynamics 2009;38:1751-1758.

TABLES

Table 1- FDE index for lateral displacement signals
(FE vs. Photogrammetry measurements)

Point		Amplitude error	Phase error	Total error
Lower Grid	2	0.07	0.14	0.21
	3	0.04	0.12	0.16
	4	0.04	0.12	0.16
	7	0.04	0.12	0.16
	8	0.07	0.09	0.16
	9	0.08	0.20	0.28
	12	0.04	0.12	0.16
	13	0.03	0.14	0.17
	14	0.07	0.14	0.21
	17	0.06	0.27	0.33
	18	0.06	0.26	0.32
	19	0.05	0.28	0.33
Upper Grid	37	0.09	0.25	0.34
	38	0.06	0.19	0.25
	39	0.09	0.28	0.37
	44	0.04	0.48	0.52
	45	0.04	0.38	0.42
	46	0.06	0.42	0.48
	51	0.07	0.36	0.43
	52	0.03	0.38	0.41
	53	0.08	0.35	0.43
	58	0.09	0.31	0.40
	59	0.08	0.40	0.48
	60	0.08	0.39	0.47

Table 2- FDE index for vertical displacement (f_y= 75 ksi)
(FE vs. Photogrammetry measurements)

FEA	Grid Point	Amplitude error	Phase error	Total error
5 in. above footing Left	3	0.13	0.64	0.77
10 in. above footing Left	7	0.11	0.63	0.74
10 in. above footing Right	9	0.12	0.64	0.76
5 in. below cap beam Left	52	0.07	0.61	0.68
10 in. below cap beam Left	44	0.08	0.62	0.70
10 in. below cap beam Right	46	0.09	0.61	0.70

Table 3- FDE index for vertical displacement (f_y = 75 ksi)
(FE vs. LVDT measurements)

FEA	LVDT	Amplitude error	Phase error	Total error
5 in. above footing Left	LVDT 3EBR7	0.23	0.35	0.58
5 in. above footing Right	LVDT 3EBR8	0.17	0.53	0.70
10 in. above footing Left	LVDT 3EBR5	0.25	0.42	0.67
10 in. above footing Right	LVDT 3EBR6	0.17	0.52	0.69
5 in. below cap beam Left	LVDT 3ETR3	0.28	0.20	0.48
5 in. below cap beam Right	LVDT 3ETR4	0.15	0.19	0.34
10 in. below cap beam Left	LVDT 3ETR5	0.09	0.24	0.33
10 in. below cap beam Right	LVDT 3ETR6	0.09	0.19	0.28

Table 4- FDE indices for models with various yield strengths
(FE vs. LVDT measurements)

Signal	Yield strength of the steel, ksi (MPa)	Amplitude error	Phase error	Total error
Vertical Displacement @ 5 in. below the cap beam	64 (441)	0.33	0.20	0.53
	70 (483)	0.30	0.20	0.50
	75 (517)	0.28	0.20	0.48
	80 (552)	0.27	0.20	0.47
Lateral Displacement @ 5 in. below the cap beam	64 (441)	0.03	0.41	0.44
	70 (483)	0.03	0.41	0.44
	75 (517)	0.03	0.38	0.41
	80 (552)	0.03	0.40	0.43
Lateral Displacement @ 12 in. below the cap beam	64 (441)	0.06	0.57	0.63
	70 (483)	0.06	0.42	0.48
	75 (517)	0.06	0.42	0.48
	80 (552)	0.05	0.41	0.46
Lateral Displacement @ 5 in. above the footing	64 (441)	0.06	0.12	0.18
	70 (483)	0.06	0.12	0.18
	75 (517)	0.04	0.12	0.16
	80 (552)	0.04	0.11	0.15
Lateral Displacement @ 12 in. above the footing	64 (441)	0.07	0.14	0.21
	70 (483)	0.07	0.14	0.21
	75 (517)	0.04	0.12	0.16
	80 (552)	0.04	0.13	0.17
Rotation @ 5 in. below the cap beam	64 (441)	0.04	0.08	0.12
	70 (483)	0.04	0.08	0.12
	75 (517)	0.04	0.08	0.12
	80 (552)	0.03	0.08	0.11
Rotation @ 12 in. below the cap beam	64 (441)	0.06	0.08	0.14
	70 (483)	0.06	0.08	0.14
	75 (517)	0.06	0.07	0.13
	80 (552)	0.04	0.07	0.11
Rotation @ 5 in. above the footing	64 (441)	0.08	0.05	0.13
	70 (483)	0.07	0.05	0.12
	75 (517)	0.05	0.05	0.10
	80 (552)	0.07	0.05	0.12
Rotation @ 12 in. above the footing	64 (441)	0.03	0.04	0.07
	70 (483)	0.03	0.04	0.07
	75 (517)	0.03	0.04	0.07
	80 (552)	0.03	0.04	0.07

All the results are for a flexural spring stiffness $K=10^8$ lb-in.

Table 5- FDE index for various values of cap beam flexural spring stiffness (FE vs. LVDT rotation calculations) (f_y= 75 ksi)

Signal	Flexural stiffness of cap beam lb-in. (N-m)	Amplitude error	Phase error	Total error
Rotation @ 5 in. below the cap beam	$1x10^8$ ($11x10^6$)	0.03	0.08	0.11
	$5x10^8$ ($57x10^6$)	0.01	0.06	0.07
Rotation @ 12 in. below the cap beam	$1x10^8$ ($11x10^6$)	0.05	0.07	0.12
	$5x10^8$ ($57x10^6$)	0.05	0.05	0.10
Rotation @ 5 in. above the footing	$1x10^8$ ($11x10^6$)	0.08	0.05	0.13
	$5x10^8$ ($57x10^6$)	0.12	0.05	0.17
Rotation @ 12 in. above the footing	$1x10^8$ ($11x10^6$)	0.11	0.05	0.16
	$5x10^8$ ($57x10^6$)	0.15	0.06	0.21

Table 6- FDE results for analyses with different stiffness of the cap beam analysis (FE vs. LVDT vertical displacement measurements)

f_y ksi (MPa)	Flexural stiffness of cap beam lb-in. (N-m)	Amplitude error	Phase error	Total error
68 (469)	$1x10^8$ ($11x10^6$)	0.41	0.20	0.61
	$1.5x10^8$ ($17x10^6$)	0.24	0.23	0.47
	$5x10^8$ ($57x10^6$)	0.11	0.33	0.44
75 (517)	$1x10^8$ ($11x10^6$)	0.28	0.20	0.48
	$5x10^8$ ($57x10^6$)	0.09	0.29	0.38

Table 7- FDE index for various combinations of stiffness recovery parameters

Signal	Stiffness recovery parameters	Amplitude error	Phase error	Total error
Rotation @ 5 in. below the cap beam	w_c=0.5, w_t=0	0.05	0.08	0.13
	w_c=0.8, w_t=0	0.05	0.08	0.13
	w_c=1, w_t=0.8	0.05	0.08	0.13
	w_c=0.8, w_t=1	0.04	0.08	0.12
Rotation @ 12 in. below the cap beam	w_c=0.5, w_t=0	0.06	0.08	0.14
	w_c=0.8, w_t=0	0.06	0.08	0.14
	w_c=1, w_t=0.8	0.06	0.08	0.14
	w_c=0.8, w_t=1	0.06	0.07	0.13
Rotation @ 5 in. above the footing	w_c=0.5, w_t=0	0.06	0.05	0.11
	w_c=0.8, w_t=0	0.06	0.05	0.11
	w_c=1, w_t=0.8	0.06	0.05	0.11
	w_c=0.8, w_t=1	0.05	0.05	0.10
Rotation @ 12 in. above the footing	w_c=0.5, w_t=0	0.04	0.04	0.08
	w_c=0.8, w_t=0	0.04	0.04	0.08
	w_c=1, w_t=0.8	0.04	0.04	0.08
	w_c=0.8, w_t=1	0.07	0.04	0.07

For all models f_y= 75 ksi (517 MPa) and cap beam flexural spring stiffness 10^8 lb-in. ($11x10^6$ N m)

FIGURES

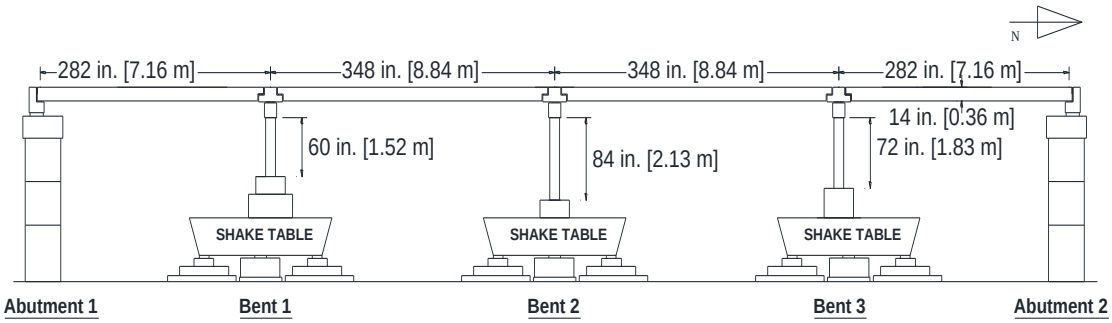

Figure 1- Elevation view of the four-span bridge

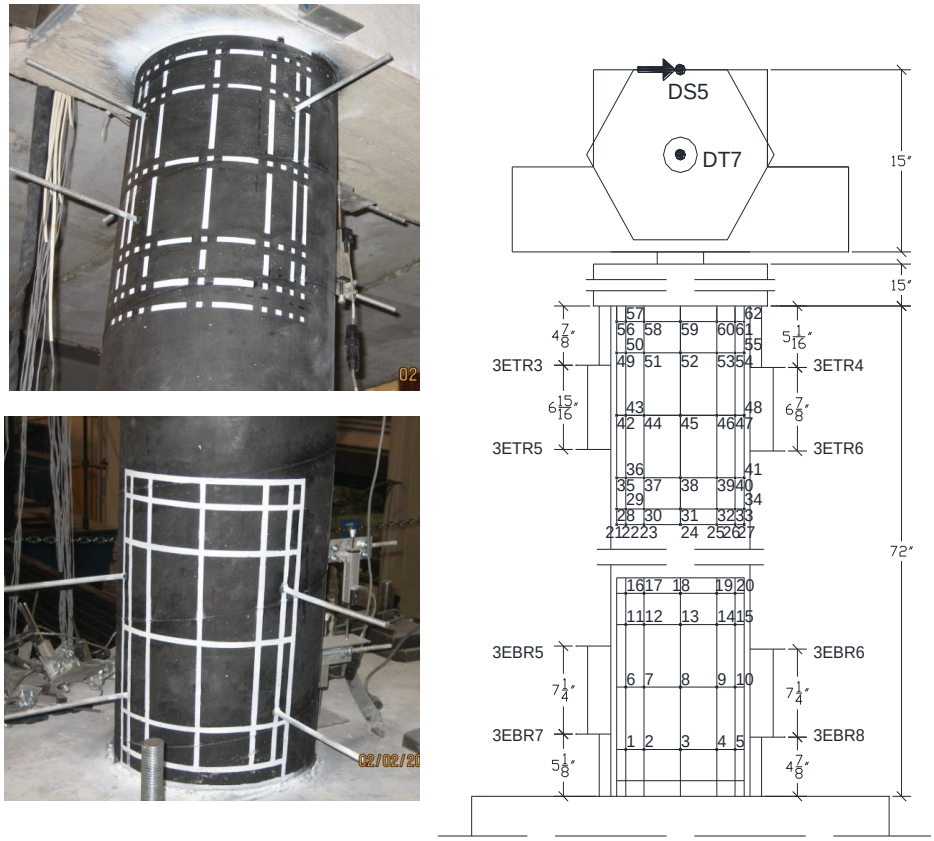

Figure 2- Bottom and top grid systems

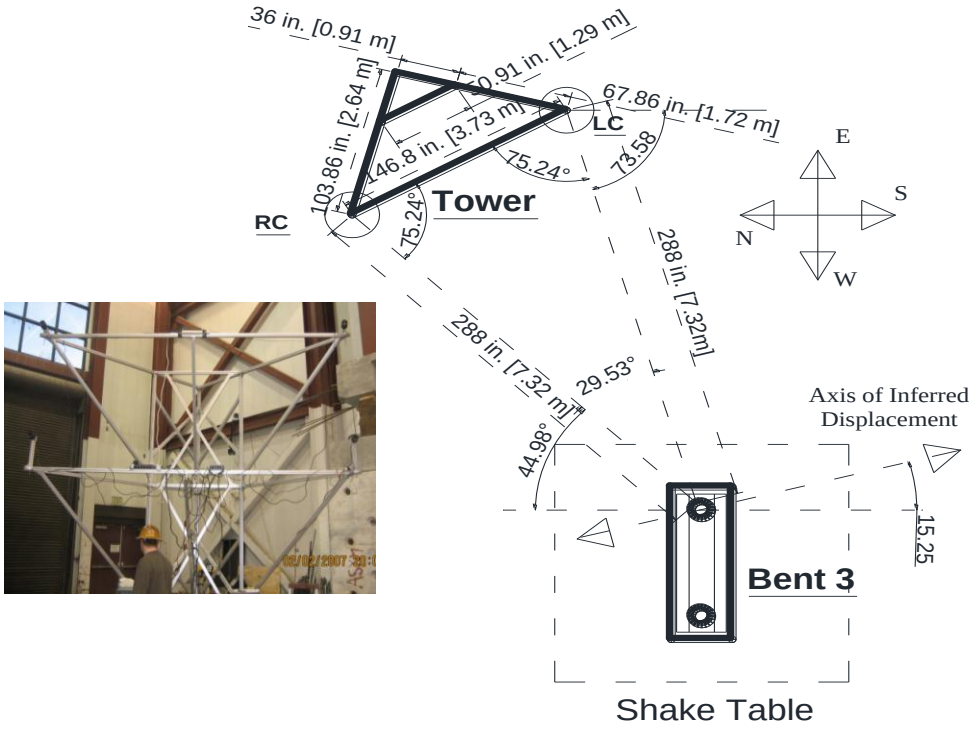

Figure 3- Location of the Bent 3 east column and the aluminum tower

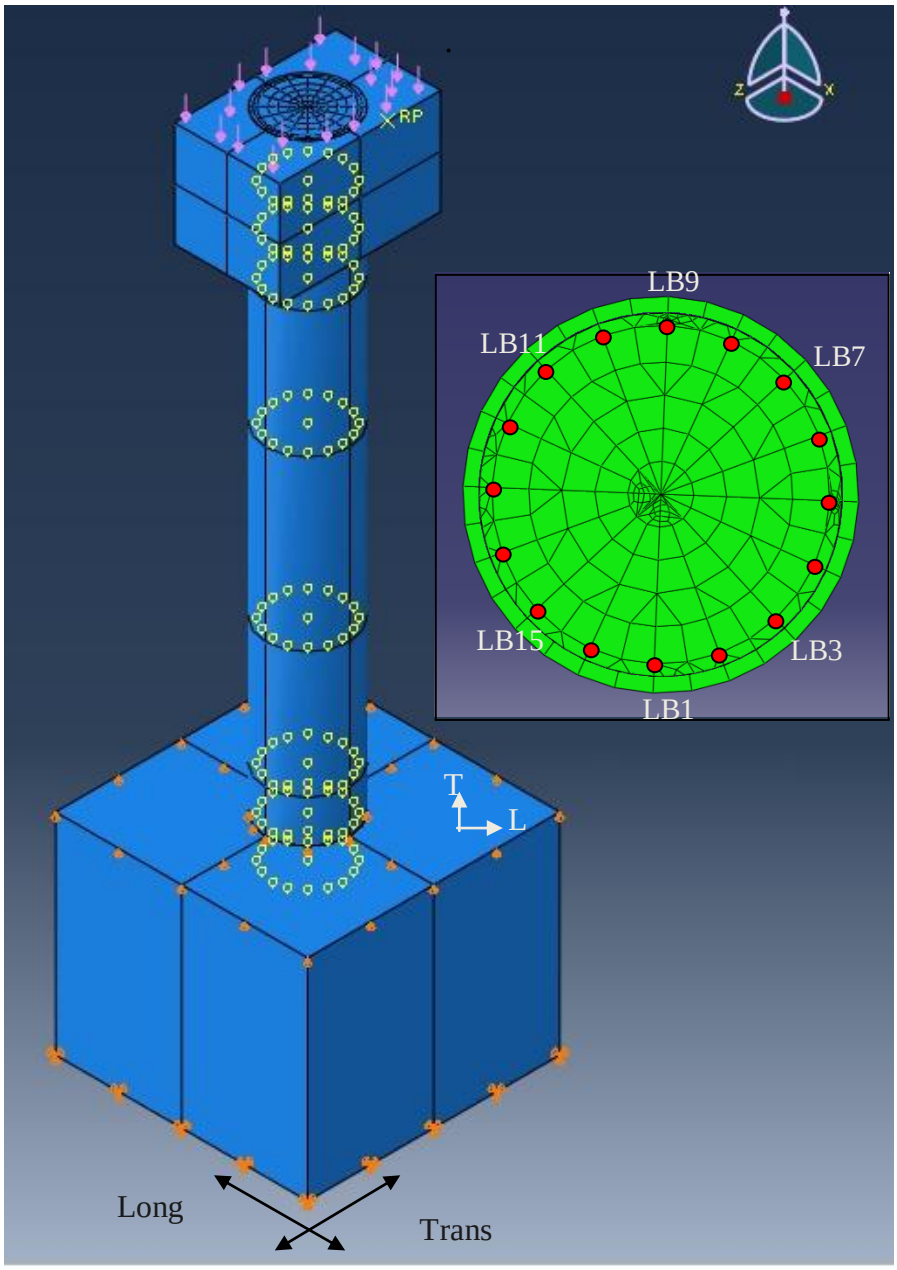

Figure 4- FE model boundary conditions and cross-sectional view of the column. RP represents the location of the rotational spring.

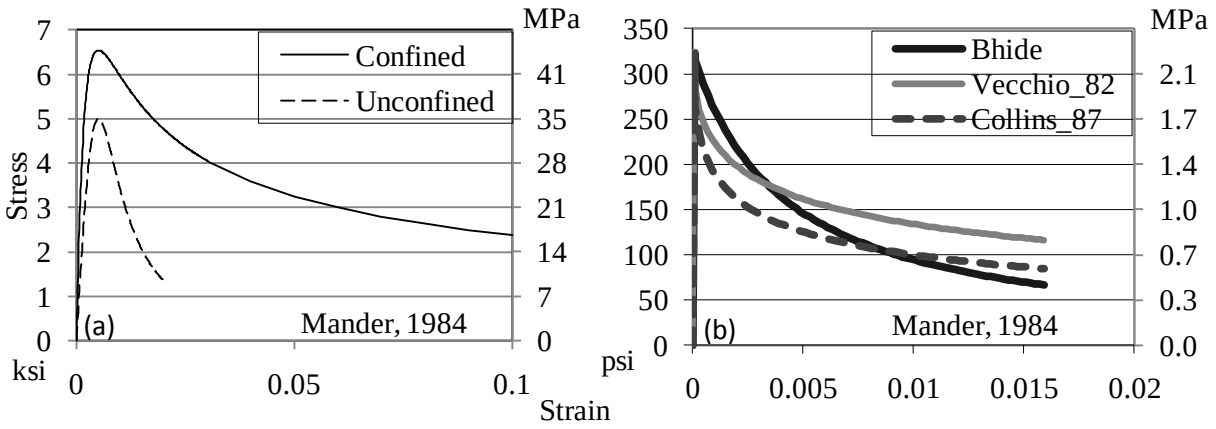

Figure 5- Concrete compression (a) and tension (b) models

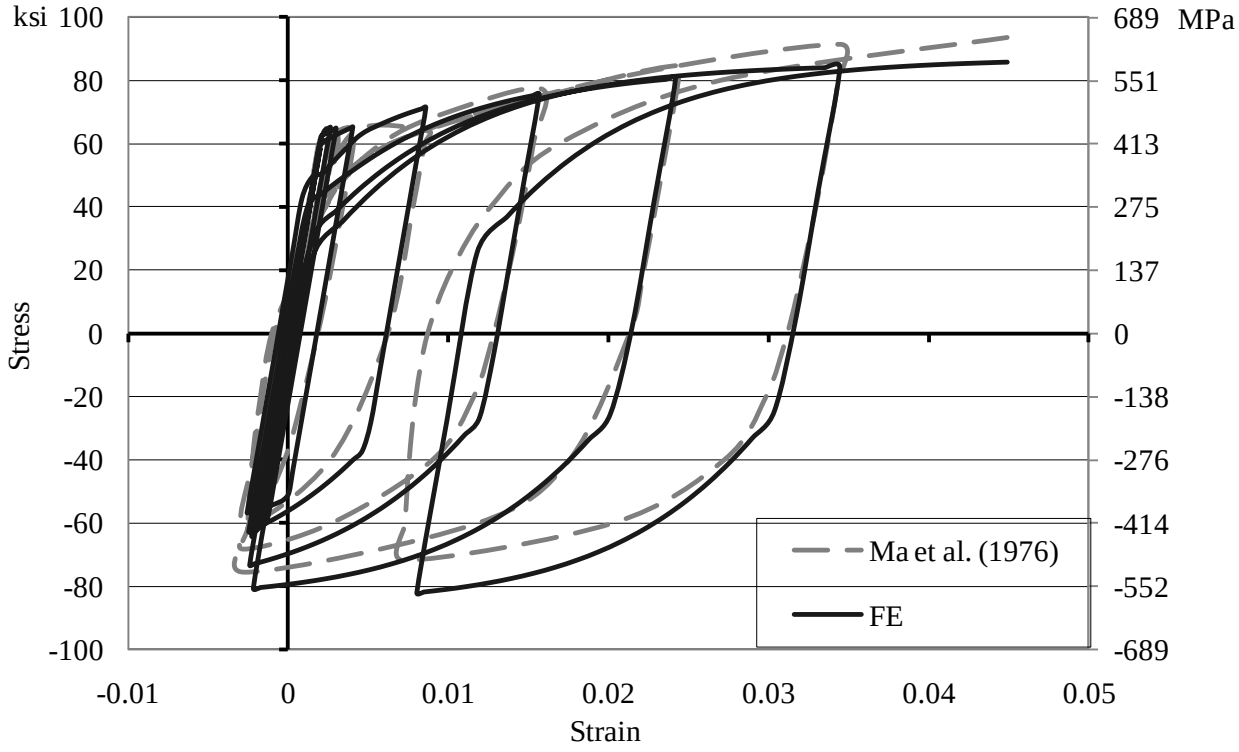

Figure 6- Comparison between computed and measured stress-strain response of reinforcing steel subjected to reversed cyclic loading (Experimental data from Ma et al. (1976))

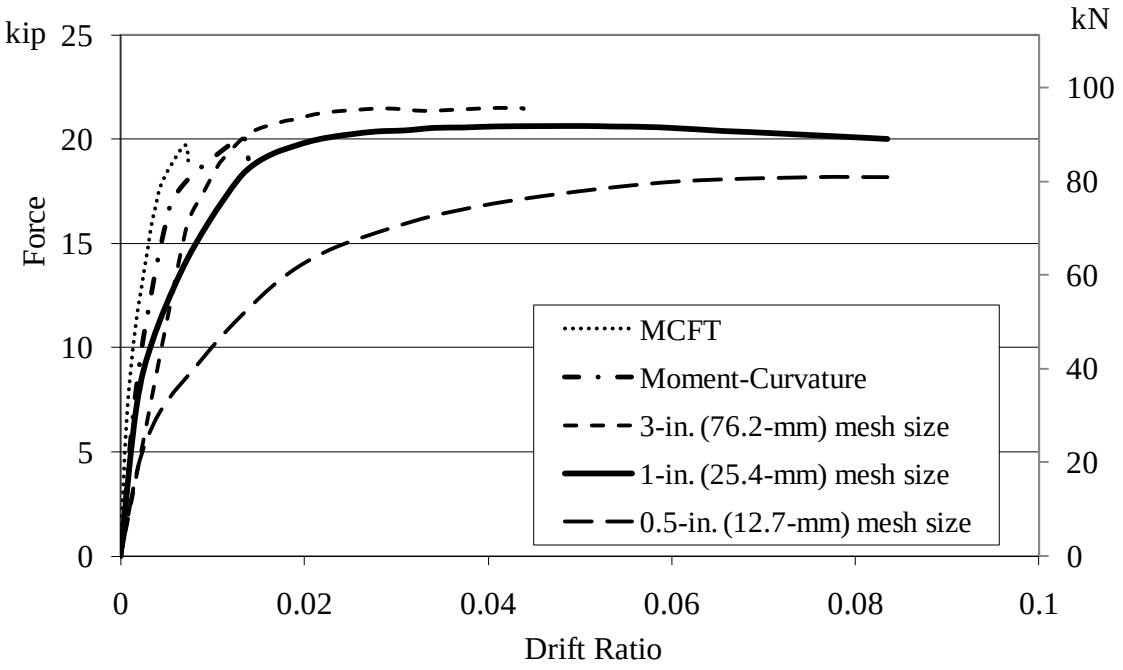

Figure 7- Load-deflection curves for monotonic loading analysis of FE model of the bridge column with various mesh densities

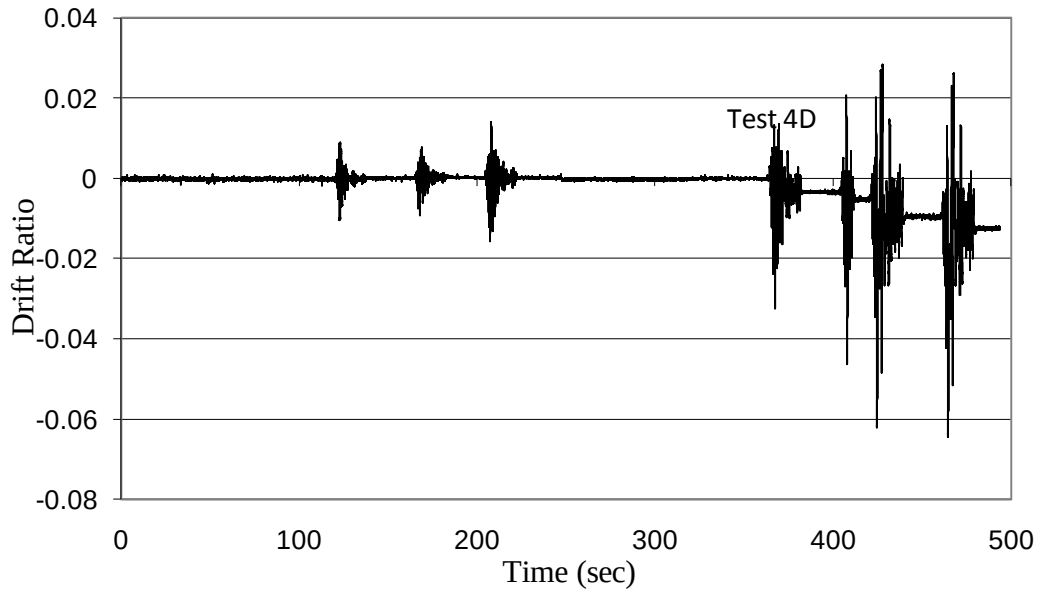

Figure 8- Displacement history recorded at the top of the bridge deck along the transverse direction for all test trials (using sensor DT7).

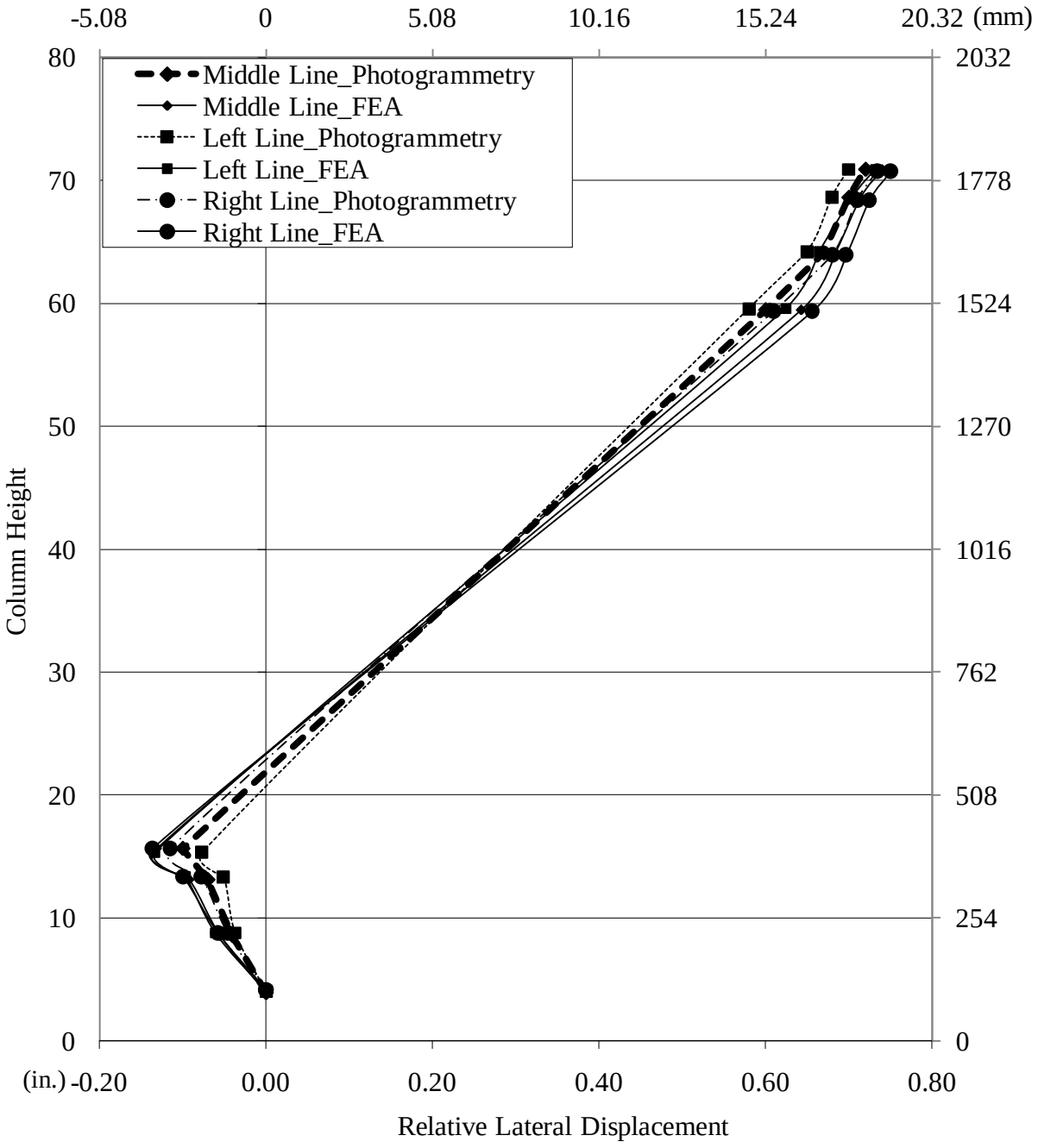

Figure 9- Deformed shape of the bridge column at the maximum drift during Test 4D with f_y=75 ksi (517 MPa), K_g=10^8 lb-in (113x10^5 N-m), w_c =0.8 and w_t =1.0.

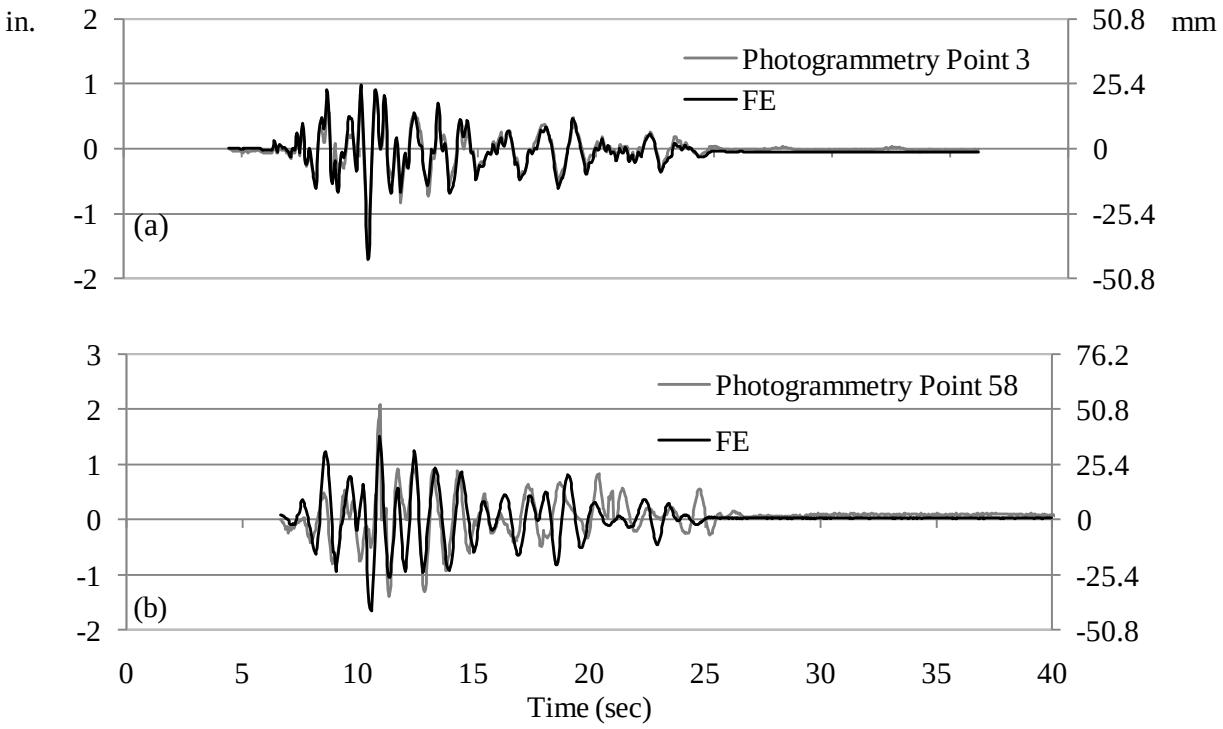

Figure 10- Comparison of lateral displacement signals between (a) Point 3 and (b) Point 58 of photogrammetry grids and FE analysis. Test 4D with f_y=75 ksi (517 MPa), K_g=10^8 lb-in (113x10^5 N-m), w_c =0.8 and w_t =1.0.

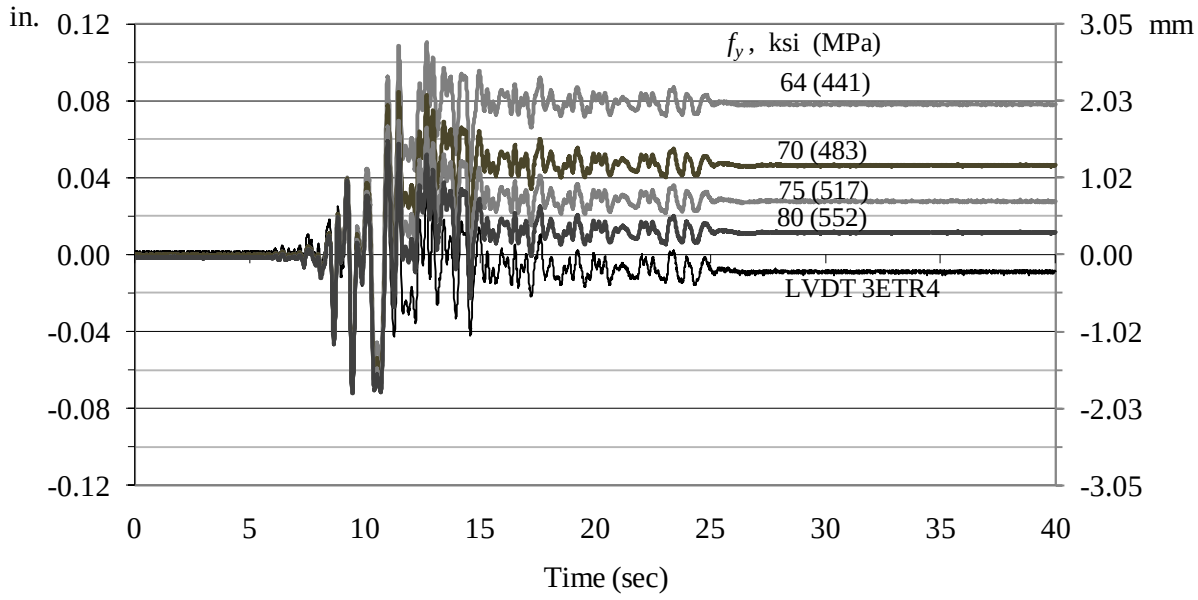

Figure 11- Comparison of vertical displacement signals between various FE models and LVDT measurements at the location of LVDT 3ETR4 (top of the column). Test 4D with K_g=10^8 lb-in (113x10^5 N-m), w_c =0.8 and w_t =1.0.

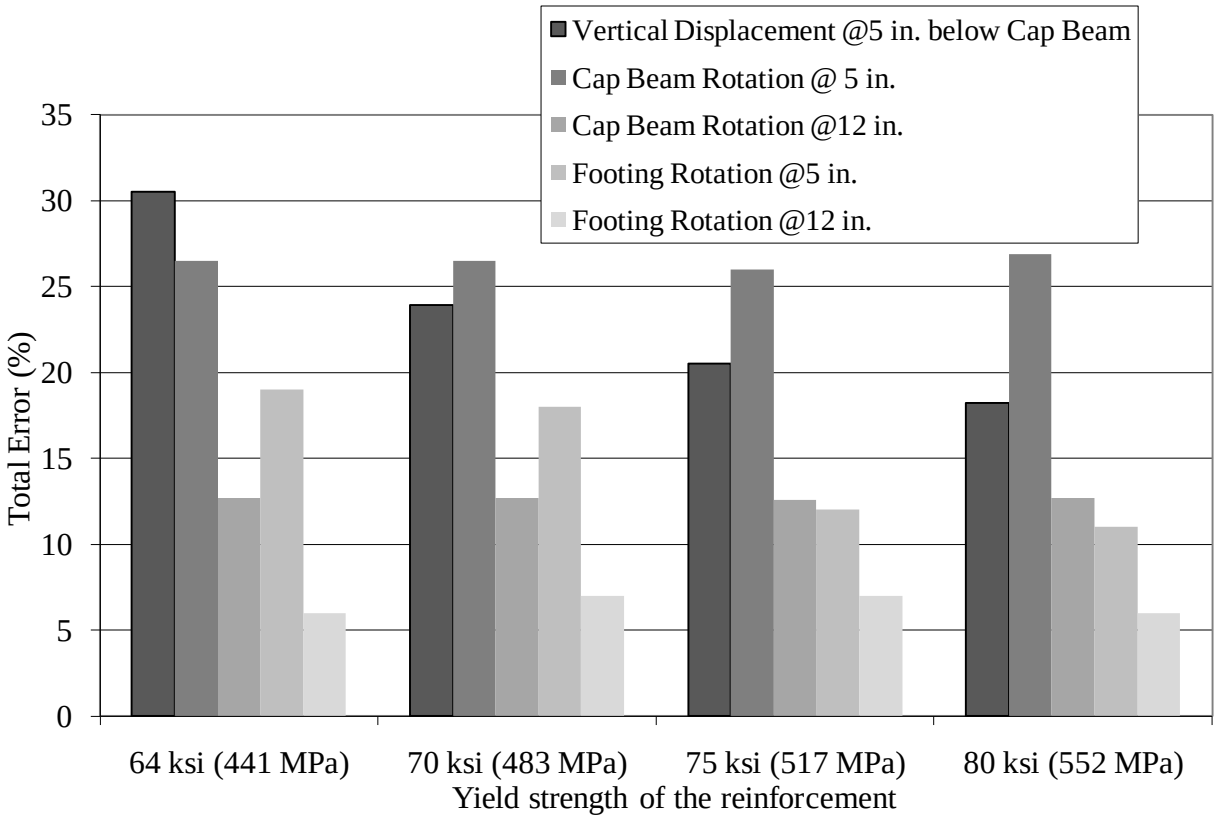

Figure 12-The comparison of FDE index errors for vertical displacement and cross-sectional rotations for different yield strength of steel. Test 4D with K_g=10^8 lb-in (113x10^5 N-m), w_c =0.8 and w_t =1.0.

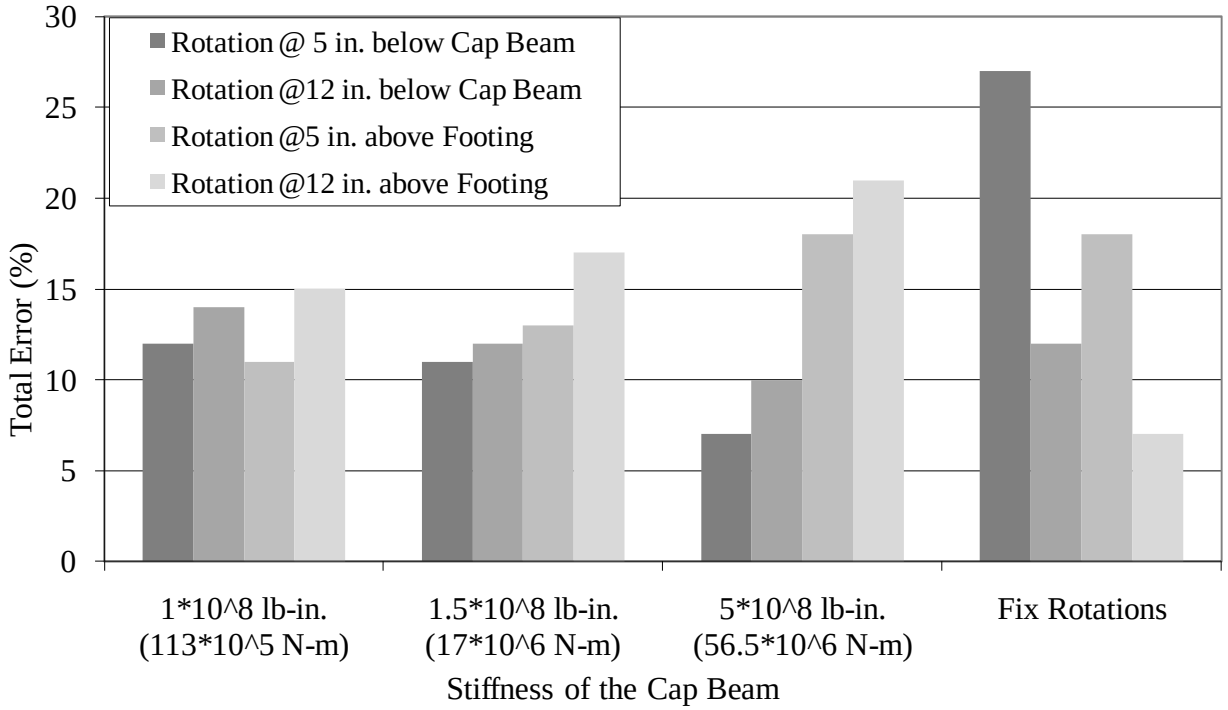

Figure 13- Comparison of FDE index errors for cross-sectional rotations for different stiffness of the cap beam. Test 4D with f_y=75 ksi (517 MPa), w_c =0.8 and w_t =1.0.

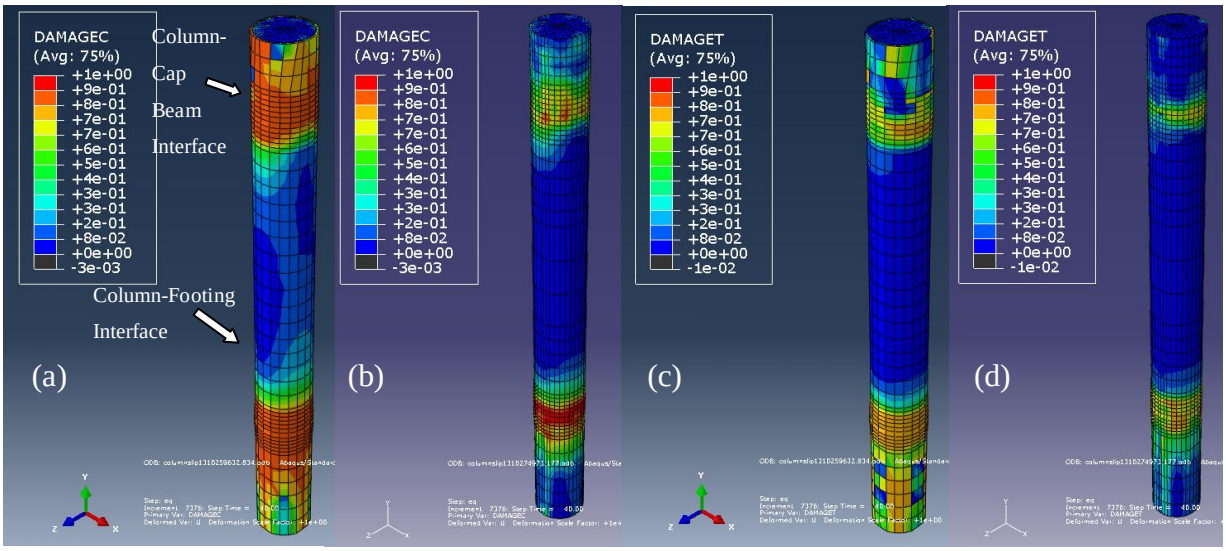

Figure 14- Computed damage indicators for concrete at the column surface: (a) compression damage, concrete shell, (b) compression damage, concrete core, (c) tension damage, concrete shell, (d) tension damage, concrete core. Test 4D with f_y=75 ksi (517 MPa), K_g=10^8 lb-in (113x10^5 N-m), w_c =0.8 and w_t =1.0.

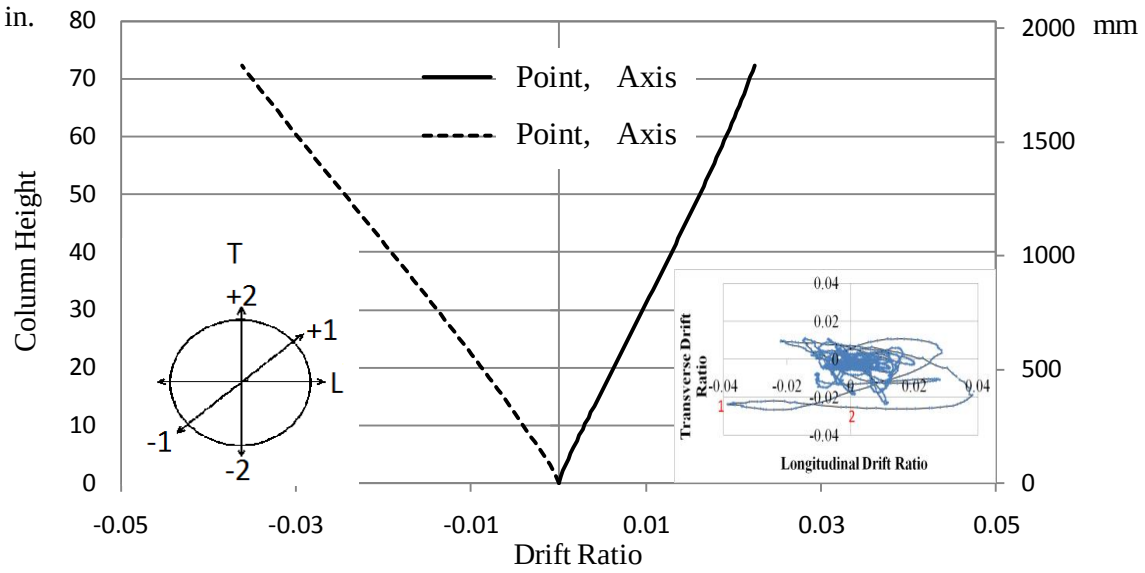

Figure 15- Computed peak displacement profiles during trial 4D. Test 4D with f_y=75 ksi (517 MPa), K_g=10^8 lb-in (113x10^5 N-m), w_c =0.8 and w_t =1.0.

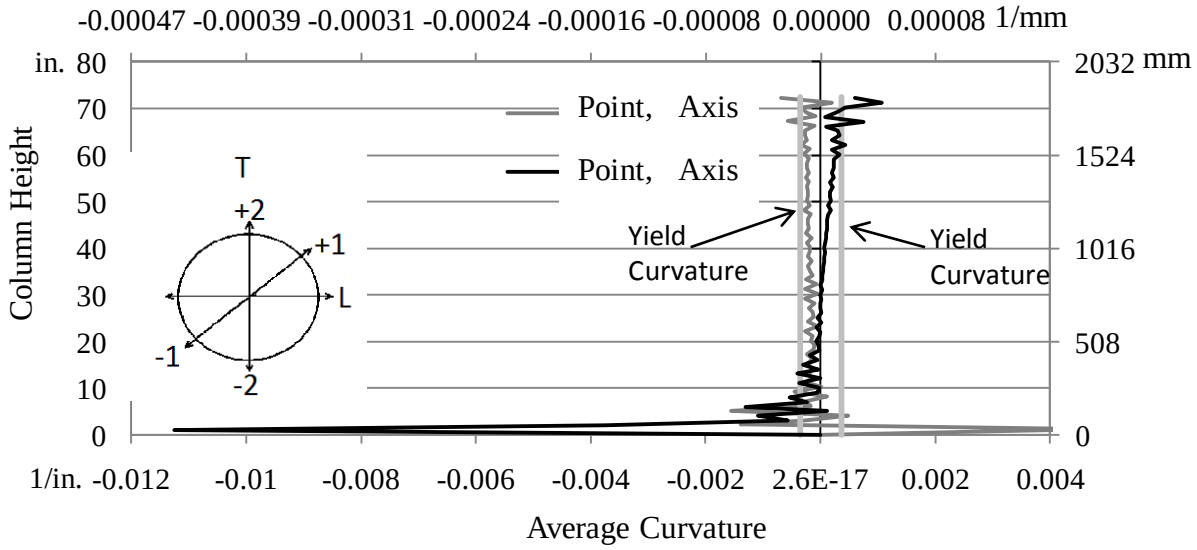

Figure 16- Computed curvature profiles at peak displacement points during trial 4D. Test 4D with f_y=75 ksi (517 MPa), K_g=10^8 lb-in (113x10^5 N-m), w_c =0.8 and w_t =1.0.

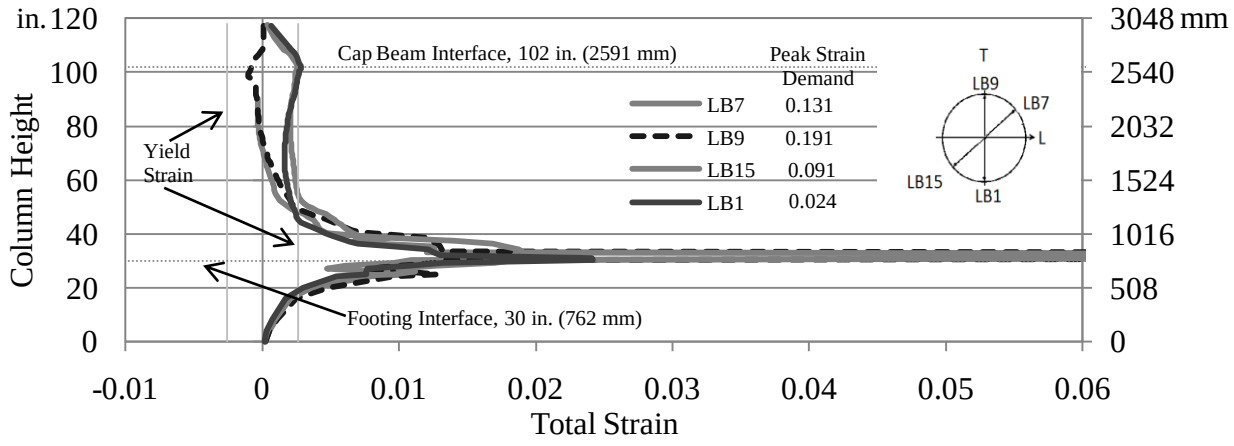

Figure 17- Computed steel strain demand along the longitudinal reinforcing bars (column, cap beam and footing) drift ratio at the peak displacement point, time=10.61 s (corresponds to Point 1 in Fig. 15).